ACS APPLIED ELECTRONIC MATERIALS

pubs.acs.org/acsaelm Article

Phase Transition and Bandgap Engineering of MgSnO Thin Films for Solar-Blind Ultraviolet Photodetector Applications

Chengyun Shou, Tianchen Yang, Theodore Yang, Abdullah Almujtabi, Yuan Li, Quazi Sanjid Mahmud, and Jianlin Liu*

Cite This: *ACS Appl. Electron. Mater.* 2024, 6, 1912−1920 Read Online

ACCESS | Metrics & More | Article Recommendations | Supporting Information

ABSTRACT: Tin oxide (SnO_2) is one of the transparent conducting oxide semiconductors that have been widely used in optoelectronic devices. To extend SnO_2-based optoelectronic applications into the deep ultraviolet solar-blind wavelength range, in this research, MgSnO alloy thin films were grown on *c*-sapphire using plasma-assisted molecular beam epitaxy. As Mg composition is between 0 and ∼24.4 at. %, MgSnO films exhibit rutile structure. The lattice constants increase as the Mg composition increases. MgSnO films become amorphous as Mg composition exceeds 24.4 at. % and eventually become rock-salt structures as Mg composition exceeds 45.9 at. %. The optical bandgap of MgSnO increases with the increase in Mg composition. Metal−semiconductor−metal (MSM) photodetector devices were fabricated and characterized. When Mg composition increases, both the dark current and photocurrent of the devices decrease. High responsivities were observed for all MgSnO MSM devices.

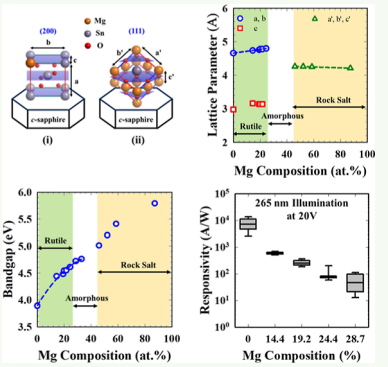

KEYWORDS: *magnesium tin oxide, phase transition, bandgap engineering, ultrawide bandgap semiconductor, metal−semiconductor−metal photodetectors*

1. INTRODUCTION

Transparent conducting oxide (TCO) semiconductors have high transmittance in the visible light range and are often used in displays, solar cells, and other optoelectronic devices.[1−3] Among these TCO semiconductors, tetragonal rutile structure tin oxide (SnO_2) has been applied in many areas such as gas sensors,[3,4] glass coating,[5] and transparent electrodes.[6,7] However, due to its relatively small bandgap (3.6 eV), it is difficult to realize a SnO_2-based deep ultraviolet (UV) applications,[8] including solar-blind photodetection of light with a wavelength below 280 nm, which requires a semiconductor of a bandgap of ∼4.4 eV or larger.[9] To enable this application, ultrawide bandgap (UWBG) semiconductor binary compounds such as AlN[10−12] and Ga_2O_3[13−17] have been explored. A recent study of Qin et al.[17] demonstrated a Ga_2O_3-based photodetector with a high responsivity of 230 A/W and a fast decay time of 24 ms. An alternative solution is to use ternary alloys, in which their bandgaps can be precisely tuned. Among these alloys, AlGaN[18−22] and MgZnO[23,24] have been studied extensively. Zhang et al.[21] demonstrated an AlGaN/GaN-based phototransistor with a high responsivity of 3.6×10^7 A/W under 265 nm illumination using a high electron mobility transistor (HEMT) configuration. In addition, our recent studies of MgGaO thin films with a bandgap larger than ∼5 eV have shown strong deep-UV photodetection performance.[25−27] In analogy to these alloys, MgSnO, which can be construed as a mixture of SnO_2 and MgO materials, is a potential candidate for solar-blind photodetection applications. In addition, the ambipolar doping characteristics of SnO and SnO_2 were reported.[28−33] Thus, combining this property and the UWBG of MgSnO together could lead to bipolar devices with both electron and hole transport in the solar blind regime.

In this perspective, Xu et al.[34] demonstrated amorphous MgSnO photodetectors with bandgaps ranging from 4.13 to 4.67 eV, which confirms the potential of using MgSnO ternary alloys to achieve deep-UV photodetectors. Compared to single-crystal material, amorphous material has multiple advantages, such as being easy to fabricate on a large scale, having no grain boundaries, and having a low fabrication cost.[35−38] However, if MgSnO could appear as a single crystalline nature instead of an amorphous nature, the device performance would be vastly improved. Moreover, the phase transition of MgSnO from rutile to amorphous and to rock-salt structure is still unclear. In this study, MgSnO thin films with different Mg compositions were grown by plasma-assisted molecular beam epitaxy (MBE), and their phase transition and

Received: December 20, 2023
Revised: February 26, 2024
Accepted: February 27, 2024
Published: March 11, 2024

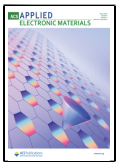

https://doi.org/10.1021/acsaelm.3c01804
ACS Appl. Electron. Mater. 2024, 6, 1912−1920

Table 1. Film Thickness, Mg and Sn Composition, Lattice Structure Parameters, and Optical Bandgap for all MgSnO Samples

sample	thickness (nm)	Mg at. %	Sn at. %	structure	XRD *d*-spacing (Å)	in-plane (002) rsm (Å)	lattice parameter (Å)	bandgap (eV)
#1	53.31	0	100	$Mg_xSn_{1-x}O_2$ (rutile)	2.33	1.49	$a = b = 4.66$ $c = 2.98$	3.89
#2	54.25	14.4	85.6	$Mg_xSn_{1-x}O_2$ (rutile)	2.37	1.58	$a = b = 4.74$ $c = 3.16$	4.44
#3	55.87	19.2	80.8	$Mg_xSn_{1-x}O_2$ (rutile)	2.38	1.57	$a = b = 4.76$ $c = 3.14$	4.48
#4	58.58	19.9	80.1	$Mg_xSn_{1-x}O_2$ (rutile)	2.39	1.57	$a = b = 4.78$ $c = 3.14$	4.54
#5	65.84	21.6	78.4	$Mg_xSn_{1-x}O_2$ (rutile)	2.39	1.57	$a = b = 4.78$ $c = 3.14$	4.55
#6	67.75	24.4	75.6	$Mg_xSn_{1-x}O_2$ (rutile)	2.40	N/A	$a = b = 4.80$	4.61
#7	71.79	28.7	71.3	$Mg_xSn_yO_z$ (amorphous)	N/A	N/A	N/A	4.72
#8	63.29	32.9	67.1	$Mg_xSn_yO_z$ (amorphous)	N/A	N/A	N/A	4.76
#9	76.00	45.9	54.1	$Mg_xSn_{1-x}O$ (rock salt)	2.46	N/A	$a' = b' = c' = 4.26$	5.01
#10	93.66	52.1	47.9	$Mg_xSn_{1-x}O$ (rock salt)	2.46	N/A	$a' = b' = c' = 4.26$	5.20
#11	109.83	58.6	41.4	$Mg_xSn_{1-x}O$ (rock salt)	2.45	N/A	$a' = b' = c' = 4.25$	5.41
#12	312.57	87.3	12.7	$Mg_xSn_{1-x}O$ (rock salt)	2.43	N/A	$a' = b' = c' = 4.21$	5.79

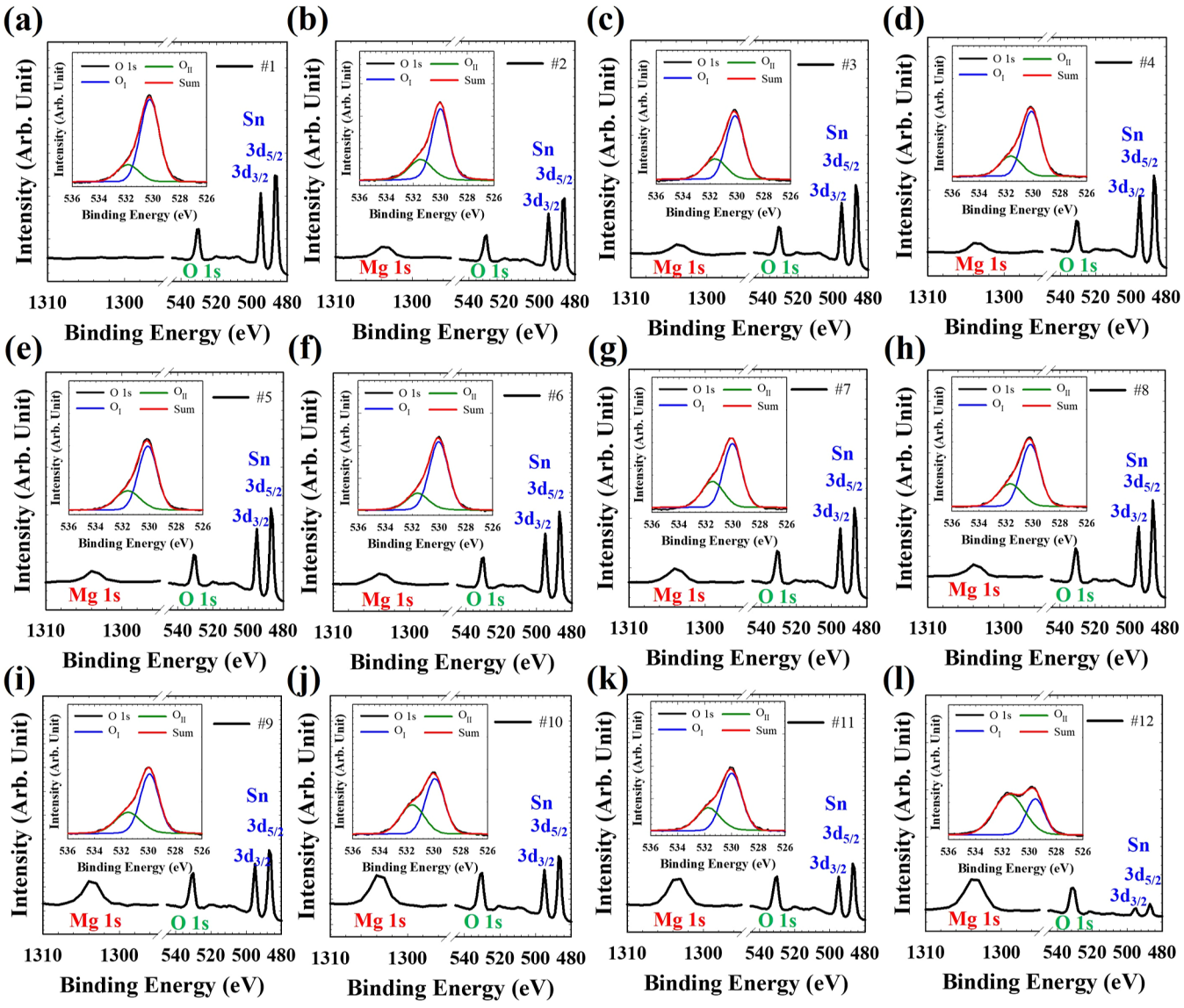

Figure 1. (a–l) XPS survey spectra and oxygen 1s peak deconvolution in the inset for all MgSnO thin films from samples 1–12.

https://doi.org/10.1021/acsaelm.3c01804
ACS Appl. Electron. Mater. 2024, 6, 1912–1920

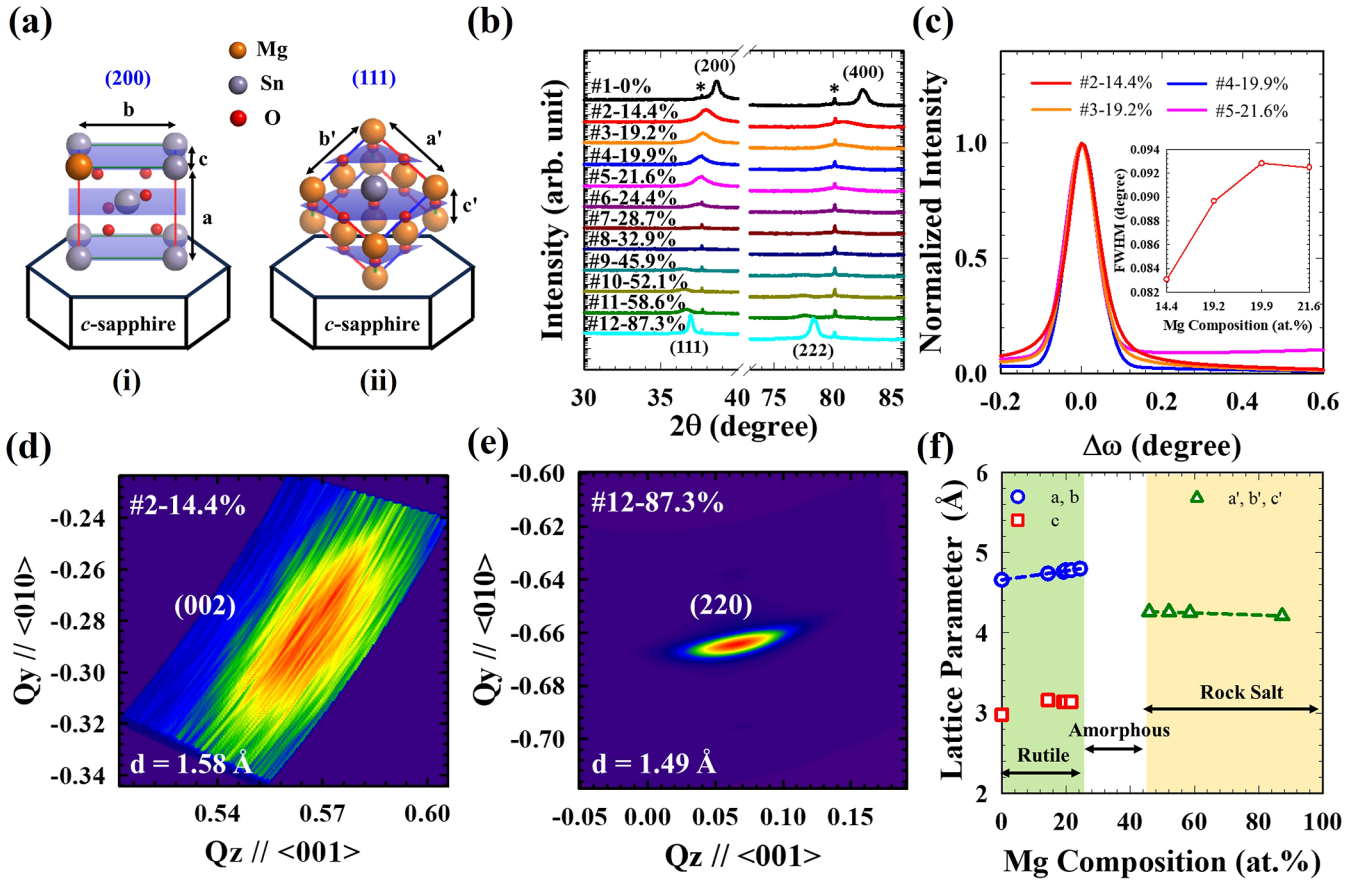

Figure 2. (a) Schematic of (i) rutile structure with (200) orientation and (ii) rock-salt structure with (111) orientation MgSnO sample grown on *c*-sapphire. (b) XRD pattern in $\theta/2\theta$ scan mode, showing the (200) orientation for rutile structure from samples 1 to 6, and the (111) orientation for rock-salt structure from samples 9 to 12. No diffraction peaks from films are observed for samples 7 and 8, an indication of an amorphous nature. (c) XRD rocking curves of the rutile structure (200) peak for samples 2−5 and the fwhm fitted using the Gaussian method are plotted in the inserted graph. In-plane rsm and the plane distance of (d) (002) plane for sample 2 and (e) (220) plane for sample 12. (f) Lattice parameters as a function of Mg composition.

bandgap engineering were studied. Metal−semiconductor−metal (MSM) photodetectors with different Mg compositions were fabricated and characterized.

2. EXPERIMENTAL SECTION

2.1. Film Growth. A 2 in. *c*-plane sapphire was cleaned by using piranha solution to remove any organic substances, then rinsed with DI water to remove residual acid from the substrate. After being blow-dried by nitrogen, *c*-plane sapphire substrate was put into the loadlock of the MBE chamber (SVT Associates, Inc.). 4 N Mg and 6 N Sn from Alfa Aesar were used for sample growth. Oxygen flow rate was set to 2.5 mbar with an RF power of 400 W. Preannealing of substrate at 800 °C for 15 min was performed, and then substrate temperature was set to 650 °C for sample growth. After that, the substrate temperature was increased to 700 °C, and a postgrowth annealing process with oxygen was carried out for 20 min.

2.2. Film Characterization. The thickness of the samples was measured using a Nikon Profilm3D profilometer. The surface morphology of MgSnO thin films was measured using the tapping mode by a Dimension 5000 atomic force microscopy (AFM) system. To analyze the Mg composition and valence band spectra for each sample, X-ray photoelectron spectroscopy (XPS) characterizations of different MgSnO thin films were carried out with a Kratos AXIS ULTRADLD XPS system using an Al Kα X-ray source. During measurement, vacuum pressure was kept below 3×10^{-9} Torr. XRD $\theta/2\theta$ scan was measured using a PANalytical Empyrean Series 2 XRD system with Cu Kα X-ray (λ = 0.15405 nm) to understand the crystal orientation. The quality of MgSnO thin films and in-plane distance were evaluated using a Rigaku SmartLab X-ray diffractometer. Absorbance and transmittance spectra of MgSnO samples were obtained using an Agilent Cary 5000 Double Beam UV/Vis/NIR spectrometer.

2.3. Device Characterization. Current−voltage (I−V) characteristics were measured on a Signatone S1045 probe station equipped with a hot chuck, an Agilent 4155C semiconductor parameter analyzer, and a 265 nm light source with a power of 420 μW. The 265 nm light source was used and controlled by a pulse generator during the current−time (I−t) measurement process. The light source was turned on for 40 s, then turned off for 70 s. The voltage applied on the photodetectors was set to 20 V, and the response current was collected using an Agilent 4155C semiconductor parameter analyzer.

3. RESULTS AND DISCUSSION

Table 1 shows the characterized parameters of MgSnO samples in this study with Mg composition ranging from 0 to 87.3 at. % and the thickness ranging from 53.31 to 312.57 nm. AFM images of the selected samples with different compositions and phases are shown in Figure S1 in the Supporting Information. The root-mean-square (RMS) roughness is estimated to be between 0.45 and 1.3 nm for these samples, indicating a smooth surface. We did not find any relationship between the Mg composition and RMS roughness, as inferred from AFM results. Figure 1 shows XPS survey spectra of Sn $3d_{5/2}$, Sn $3d_{3/2}$, and Mg 1s for all MgSnO samples, and the inset graph shows the O 1s peak

https://doi.org/10.1021/acsaelm.3c01804
ACS Appl. Electron. Mater. 2024, 6, 1912−1920

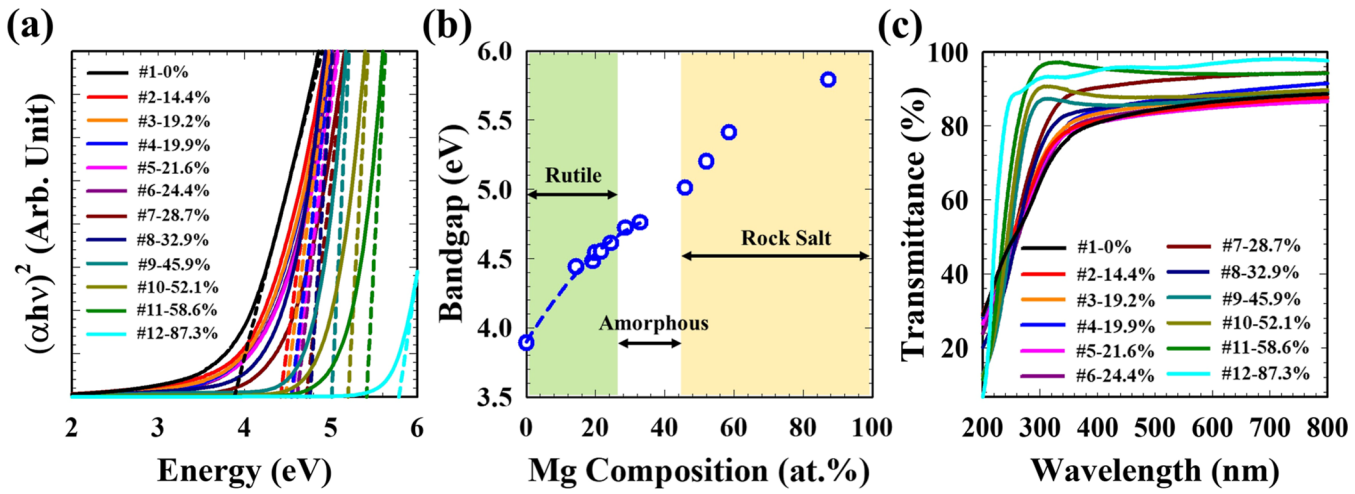

Figure 3. (a) Tauc plot absorption spectra of all MgSnO samples. (b) Bandgap vs Mg composition plot. (c) Transmittance spectra of all MgSnO samples.

deconvolution. Peaks with binding energies located at ∼486.5 and ∼494.9 eV correspond to Sn $3d_{5/2}$ and Sn $3d_{3/2}$, respectively, which reveals the Sn^{4+} state in all MgSnO samples.[39,40] The binding energy difference of the two Sn 3d doublets is ∼8.4 eV, indicating a good agreement with the reference data.[40] The peak at a binding energy of ∼1303 eV corresponds to Mg 1s.[41,42] The peak areas for Sn 3d and Mg 1s were extracted to calculate the composition for each sample and are listed in Table 1. In the insets of Figure 1a–k, two peaks at O_I ∼ 530.1 eV and O_{II} ∼ 531.6 eV are observed for sample 1 to sample 11, which correspond to Sn–O bonds and oxygen vacancies, respectively.[39] For sample 12, the Mg–O bond located at ∼529 eV is observed, indicating that the Mg–O bond becomes the majority bond, as shown in the inset of Figure 1l. Fermi level locations were also extracted from XPS spectra and are shown in Figure S2 in the Supporting Information. The Fermi level is 2.46 eV above the valence band for sample 1, indicating the n-type nature of the film. As the Mg concentration increases, the Fermi level shifts toward the valence band.

MgSnO thin films with low and high Mg compositions could possess rutile and rock-salt phases, respectively. Figure 2a shows schematic of (i) rutile and (ii) rock-salt MgSnO films grown on *c*-sapphire substrates, respectively. However, samples with moderate Mg and Sn contents could have mixed phases or even appear as amorphous. To reveal the crystal structures and phases of the MgSnO samples, X-ray diffraction (XRD) characterizations were performed. Figure 2b shows XRD pattern in $\theta/2\theta$ scan mode, and peaks located at ∼37.7 and ∼80.1° are the background signal, which is confirmed by measuring the substrate only. For sample 1, 2θ peaks located at 38.5 and 82.3° correspond to (200) and (400) orientations of rutile structure,[43] indicating that the film has a growth direction of ⟨200⟩ along ⟨0001⟩ *c*-sapphire, as schematically shown in Figure 2a. As the Mg composition increases, the (200) peak location shifts toward a lower angle. When Mg composition exceeds 21.6 atom %, the (200) peak starts to disappear from sample 5 to sample 6. No peaks are observed from the $\theta/2\theta$ scan results of samples 7 and 8, indicating that these films are amorphous. As Mg composition continues to increase beyond 45.9 at. %, the rock-salt structure (111) peak starts to emerge and shifts toward a higher angle. For example, 2θ peaks of 36.9 and 78.4° observed for sample 12 correspond to (111) and (222) orientations of rock-salt structure,[44] as schematically shown in Figure 2a. Because the phase of MgSnO thin films transforms from rutile to amorphous and to rock salt as Mg composition increases, the chemical formulas of the films can be referred to as $Mg_xSn_{1-x}O_2$, $Mg_xSn_yO_z$, and $Mg_xSn_{1-x}O$, respectively, where *x*, *y*, and *z* are respective elemental atomic compositions.

The quality of the MgSnO films was evaluated by XRD rocking curve measurements. Figure 2c shows normalized XRD rocking curves of rutile samples 2–5, and the Gaussian method was fitted to extract the full width at half-maximum (fwhm). The fwhm of samples 2–5 is 0.0831, 0.0897, 0.0928, and 0.0925°, respectively. These small values suggest that our samples have high quality.[45] Among these samples, however, when Mg composition increases, the film becomes more disordered due to its transformation from rutile phase to amorphous, resulting in the increase of the fwhm, as shown in the inset of Figure 2c.

Next, we extracted the lattice parameters of crystalline MgSnO samples. We designate *a*, *b*, and *c* as the lattice constants for rutile MgSnO and *a*′, *b*′, and *c*′ as the lattice constants for rock-salt MgSnO. These parameters are illustrated in the schematic in Figure 2a. According to Bragg's law, $2d \sin\theta = n\lambda$, where *d* is the distance between the two planes, θ is the incident beam angle from the scatter plane, *n* is the diffraction order, and λ is the wavelength of the X-ray. The *d*-spacing values can be obtained from the XRD $\theta/2\theta$ scan results for (200) planes of rutile and (111) planes of rock-salt samples, which are listed in Table 1. With these *d*-spacing values, lattice parameters *a* and *b* of rutile MgSnO films ($a = b$) and *a*′, *b*′, and *c*′ of rock-salt MgSnO films ($a' = b' = c'$) can be extracted, and they are listed in Table 1. To obtain the *c* lattice parameter of rutile MgSnO samples, XRD in-plane reciprocal space mapping (rsm) characterizations are needed. Figure 2d shows the XRD rsm results for the (002) plane of sample 2, and Figure S3 in the Supporting Information shows in-plane rsm for the (002) plane of samples 1, 3, 4, and 5. For rutile samples, because the lattice parameter *c* is twice the in-plane distance of (002) plane, the calculated lattice parameters in the *c* direction for samples 1–5 are 2.98, 3.16, 3.14, 3.14, and 3.14 Å, respectively, which are listed in Table 1. In-plane rsm for sample 6 was not obtainable due to the disorder of the film toward the amorphous structure. In-plane rsm was also

https://doi.org/10.1021/acsaelm.3c01804
ACS Appl. Electron. Mater. 2024, 6, 1912–1920

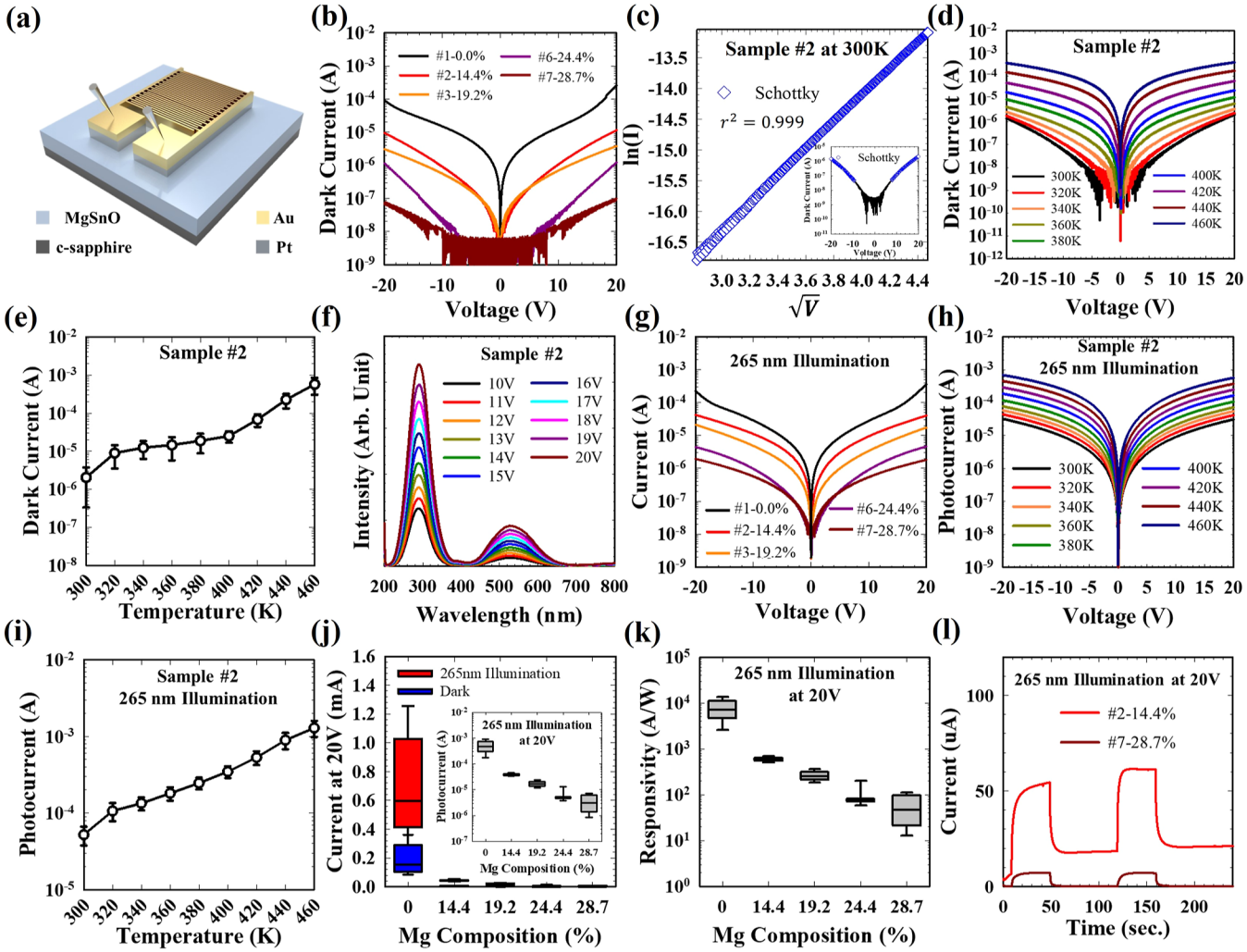

Figure 4. (a) Schematic of the interdigitated MSM photodetector with a Pt/Au electrode. (b) $I-V$ plot under dark conditions. (c) Schottky conduction current fitting for sample 2 under dark condition. The inserted plot shows the section fitted using the Schottky model. (d) Temperature-dependent $I-V$ plot for sample 2 under dark conditions with temperatures ranging from 300 to 460 K. (e) Dark current error plot extracted at 20 V with different temperatures. (f) Photocurrent spectra of the device sample 2 under different voltages and wavelengths. (g) $I-V$ plot under 265 nm illumination. (h) Temperature-dependent photocurrent−voltage plot for sample 2 under 265 nm illumination with temperatures ranging from 300 to 460 K. (i) Photocurrent error plot extracted at 20 V with different temperatures. (j) Total current under 265 nm illumination and the dark current box plot for samples with different Mg compositions. The inset box plot shows the photocurrent under 265 nm illumination. (k) Responsivity under 265 nm illumination at 20 V. (l) $I-t$ curves under 265 nm illumination for rutile sample 2 and amorphous sample 7.

performed on selected rock-salt samples to double check the lattice constants. Figure 2e shows the rsm result of the (220) plane of sample 12, and the in-plane distance of (220) is estimated as 1.49 Å, leading to a lattice parameter in the c' direction of 4.21 Å, which is consistent with the result obtained from the $\theta/2\theta$ scan. Figure 2f shows a plot of the lattice parameters as a function of the Mg composition. For rutile structure samples, as Mg composition increases, lattice parameters along a and b direction expand and are followed by a linear relationship $a = b = 4.66 + 0.00568 \times$ (Mg at. %). The lattice parameter along the c direction does not change much as the change of Mg composition. In rock-salt-structured samples, as Mg composition increases, the lattice parameters a', b', and c' reduce and are followed by a linear relationship $a' = b' = c' = 4.32-0.00129 \times$ (Mg at. %).

Absorbance spectra of MgSnO samples were obtained and converted to absorption coefficient using the equation[25] $\alpha = 2.303 \times \frac{A}{t}$, where α is the absorption coefficient, A is the absorbance obtained from the spectrometer, and t is the film thickness in centimeters. Figure 3a shows the Tauc plot absorption spectra of all MgSnO samples. Optical bandgap can be extracted from the x-axis intercept of Tauc plot using the equation $(\alpha h\nu)^2 = c\,(h\nu - E_g)$, where h is Planck's constant, ν is the frequency, c is constant, and E_g is the optical bandgap. Here, linear regression with $r^2 = 0.999$ was fitted to extract the optical bandgap of each sample. Figure 3b shows the relationship between the optical bandgap and Mg composition. As Mg composition increases, optical bandgap increases. In the rutile $Mg_xSn_{1-x}O_2$ samples, the bandgap with a unit of eV can be fitted using the equation: $E_g(x) = 3.89 + 0.04x$, where x is Mg at. %. Transmittance data T was calculated using the equation: $A = 2 - \log(\%\ T)$, where A is the absorbance, and the spectra are shown in Figure 3c. All samples show a high transmittance exceeding ~80% in the visible light range.

To explore the photodetection performance of these MgSnO thin films, MSM photodetectors were fabricated by

https://doi.org/10.1021/acsaelm.3c01804
ACS Appl. Electron. Mater. 2024, 6, 1912−1920

patterning an interdigitated Pt (20 nm)/Au (100 nm) electrode on the films, as shown in the schematic of Figure 4a. The metal contact fingers of the MSM photodetector are 220 μm long, 5 μm wide, and 3 μm in spacing with 15 fingers on both sides. Here, we report devices based on both rutile and amorphous MgSnO thin films only but not for those based on rock-salt MgSnO thin films because these rock-salt MgSnO films were found extremely insulating. Figure 4b shows the $I-V$ characteristics from −20 to 20 V for samples 1, 2, 3, 6, and 7 under dark conditions. Relatively symmetric characteristics are observed for all samples, and the current increases with the increase in the applied voltage in both polarities. As Mg composition increases from samples 1 to 7, the dark current decreases under the same voltage. An MSM device can be considered as two metal−semiconductor (MS) junctions connected in series. Under any applied bias, the MSM device contains a forward-biased MS junction and a reverse-biased MS junction. The current flowing through the MSM device is limited by the reverse-biased MS junction. At moderate and larger bias, the Schottky conduction with a consideration of image-force lowering is assumed, and the current density J can be given by[46,47]

$$J = A^*T^2\exp\left[\frac{-q(\phi_B - \sqrt{qE/4\pi\varepsilon_s})}{kT}\right] \quad (1)$$

where A^* is effective Richardson constant, T is temperature, q is electron charge, ϕ_B is Schottky barrier height, and k is Boltzmann's constant. The term $\sqrt{\frac{qE}{4\pi\varepsilon_s}}$ is image force lowering, where E is electric field, and ε_s is permittivity of the semiconductor. Here, we assume that the voltage applied across the two junctions is approximately equal to the voltage applied to the reverse bias junction. Based on the Schottky conduction equation, $\ln(I)$ is proportional to $V^{1/2}$, and the current increases as the temperature increases. Figure 4c shows the current fitting $\ln(I)$ vs $V^{1/2}$ plot for sample 2 at 300 K under a voltage range of −9.44 to −20 V, and the linear regression fitting exhibits r^2 = 0.999. The inserted graph in Figure 4c shows the $I-V$ characteristics of sample 2 that was fitted using the above Schottky conduction model. Although the Schottky conduction model can reasonably explain the dark $I-V$ characteristics for rutile MgSnO MSM devices, it is noted that the current transport can also be contributed by other mechanisms, including generation currents from defects, carrier replenishment from electrodes, trap-assisted band-to-band tunneling, etc. In the amorphous MgSnO MSM devices, as seen from the fitting results for sample 7 in the Supporting Information Figure S4, hopping current transport was also possible. Figure 4d shows temperature-dependent $I-V$ characteristics ranging from 300 to 460 K for sample 2 under dark conditions, and Figure 4e shows the dark current error plot of sample 2 by measuring over 10 data points at a voltage of 20 V. The current increases as the temperature increases, which confirms the positive correlation between the temperature and the dark current in the above equation.

Figure 4f shows the photocurrent spectra from 200 to 800 nm under different voltages for sample 2. Two peaks are observed at ∼287 and ∼526 nm. The peak at ∼287 nm (∼4.3 eV) may be due to band-to-band absorption process, and the peak at ∼526 nm (∼2.4 eV) may correspond to optical transitions involving oxygen vacancies.[48,49] Figure S5 in the Supporting Information shows similar photocurrent spectra of other samples (samples 3, 6, and 7). The rejection ratio of samples 2 and 7 at 250 and 400 nm (R_{250nm}/R_{400nm}) is obtained from the responsivity spectra at 10 V on the MSM photodetector, as seen in Figure S6. The calculated rejection ratio for 2 and 7 is 893.49 and 1642.44, respectively. Sample 7 has a larger bandgap than sample 2, which results in a higher rejection ratio. Figure 4g shows the $I-V$ characteristics of samples 1, 2, 3, 6, and 7 under 265 nm illumination. Compared with the dark current levels, as shown in Figure 4b, the currents under illumination have increased for each device, indicating the formation of photocurrents. Figure S7 shows the power-dependent photocurrent measurement results of samples 2 and 7. A 265 nm light source with an incident power of 9.89, 37.33, and 63.79 μW was used to illuminate the photodetectors. Current increases as the power increases in both samples 2 and 7. This is because higher light intensities will generate more electron−hole pairs, resulting in a higher photocurrent. Figure 4h shows temperature-dependent photocurrent−voltage characteristics of sample 2 under 265 nm illumination, and the photocurrent increases as the temperature increases. Figure 4i shows the photocurrent error plot of sample 2 by measuring over 10 devices, which confirms the increase in photocurrent at higher temperature. Figure S8 in the Supporting Information shows a similar temperature-dependent photocurrent−voltage plot and error plot by measuring over 10 devices for other samples. The temperature-dependent photocurrent results may be due to the fact that photogenerated carriers move faster under higher temperatures. In addition, temperature-dependent detrapping of the photogenerated carriers may have played a role.[50]

Figure 4j shows dark current and total current under a 265 nm illumination box plot versus different Mg compositions, and the inserted box plot shows photocurrent as a function of Mg compositions. Both dark current and photocurrent decrease with the increase in Mg composition. MgSnO with a higher Mg composition has wider optical bandgap, in turn, it results in larger Schottky barrier height, which is responsible for smaller dark current. The generation of photocarriers will be less in MgSnO samples with wider bandgap under the same excitation wavelength, leading to less photocurrent. The responsivity is calculated using $R_\lambda = \frac{\Delta I}{P}$, where ΔI is the photocurrent and P is the incident light power illuminating the semiconductor. The effective area for all devices is 1.116×10^4 μm^2, and the total incident power onto MSM devices is calculated to be 66.2 nW. Figure 4k shows the responsivity box plot of MSM samples with different Mg compositions. For Mg composition at 0, 14.4, 19.2, 24.4, and 28.7 at. %, the average responsivity is ∼7226, ∼596, ∼253, ∼75, and ∼45 A/W, respectively. Responsivity decreases as the bandgap increases with the Mg composition. This is reasonable since more photocarriers are generated in the narrower-bandgap materials, contributing to higher photocurrents. As a comparison, other wider-bandgap materials such as $MgGa_2O_4$[51] and AlGaN[52] based photodetectors exhibit a lower responsivity of 0.89 and 0.19 A/W, respectively. Nevertheless, this does not mean that wider-bandgap MgSnO semiconductors are inferior to narrower-bandgap SnO_2 semiconductors for photodetection applications. Generally, when higher-energy photons are the target to detect, photodetectors based on wider bandgap semiconductors have better signal-to-noise performance since lower-energy photons will not be absorbed. In addition, they also perform better in higher-radiation and higher-temperature

https://doi.org/10.1021/acsaelm.3c01804
ACS Appl. Electron. Mater. 2024, 6, 1912−1920

environments. While these moderate responsivity numbers are acceptable, much higher responsivities can be achieved by improving the film quality using a buffer layer,[25] using different electrodes,[53] or by fabricating avalanche photodetectors.[54,55]

Figure 4l shows the $I-t$ characteristics of the MSM photodetector samples 2 and 7, representing the devices based on rutile and amorphous MgSnO, respectively. The currents of both devices increase after the light is turned on and quickly reach plateau. After the light is turned off, the currents decrease sharply to the levels that are consistent with the dark currents in the $I-V$ measurement in Figure 4b. The rise time for samples 2 and 7 is calculated to be 1.33 and 3.45 s, respectively. The fall time, which is defined as the time duration for the change when the current decays to its value of $1/e$, was fitted using the equation: $I = I_0 e^{-t/\tau}$, where I is the current, I_0 is the photocurrent at the steady state, t is the time, and τ is the lifetime of the carriers. The fall times for samples 2 and 7 are 1.78 and 1.51 s, respectively. The response time of the photodetector is mainly affected by carrier trapping of the defects inside the film. High-quality films have fewer defects, which results in a longer response time. These numbers suggest that rutile samples have higher crystal quality than amorphous samples.[25]

4. CONCLUSIONS

In this research, we have comprehensively studied wide-bandgap MgSnO semiconductors in terms of phase transition, bandgap engineering, and their photodetector device applications. MgSnO thin films with different Mg compositions ranging from 0 to 87.3 at. % were grown using plasma-assisted MBE. MgSnO are rutile, amorphous, and rock-salt structures when Mg compositions are less than ∼24.4%, between 24.4 and 45.9%, and larger than ∼45.9%, respectively. For rutile structure samples, as Mg composition increases, lattice parameters along the a and b directions expand, and the lattice parameter along the c direction does not change much. In rock-salt-structured samples, as Mg composition increases, the lattice constant decreases slightly. Crystalline MgSnO thin films with a lower Mg composition have high quality, as revealed by XRD rocking curves. The optical bandgap increases with the increase in Mg composition and can be summarized as $E_g(x) = 3.89 + 0.04x$ for rutile samples. MSM photodetectors based on rutile and amorphous MgSnO samples were fabricated and characterized. Mg composition- or bandgap-dependent photoresponse was studied. Rutile samples have a higher responsivity but a slower response time compared to amorphous samples. High photoresponsivity and excellent $I-t$ characteristics among the MgSnO photodetector samples suggest that MgSnO thin films are promising for deep-UV solar-blind photodetection and other photonic and electronic applications.

■ ASSOCIATED CONTENT

Supporting Information

The Supporting Information is available free of charge at https://pubs.acs.org/doi/10.1021/acsaelm.3c01804.

AFM images, XPS spectra, in-plane rsm images, photocurrent $I-V$ characteristics, and photocurrent spectra of the samples with different Mg compositions (PDF)

■ AUTHOR INFORMATION

Corresponding Author

Jianlin Liu − *Department of Electrical and Computer Engineering, University of California, Riverside, California 92521, United States;* orcid.org/0000-0001-6513-0867; Phone: 1-9518277131; Email: jianlin@ece.ucr.edu; Fax: 1-9518272425

Authors

Chengyun Shou − *Department of Electrical and Computer Engineering, University of California, Riverside, California 92521, United States*

Tianchen Yang − *Department of Electrical and Computer Engineering, University of California, Riverside, California 92521, United States;* orcid.org/0000-0002-0991-471X

Theodore Yang − *Department of Electrical and Computer Engineering, University of California, Riverside, California 92521, United States; Martin Luther King High School, Riverside, California 92508, United States*

Abdullah Almujtabi − *Department of Electrical and Computer Engineering, University of California, Riverside, California 92521, United States*

Yuan Li − *Department of Electrical and Computer Engineering, University of California, Riverside, California 92521, United States*

Quazi Sanjid Mahmud − *Department of Electrical and Computer Engineering, University of California, Riverside, California 92521, United States*

Complete contact information is available at: https://pubs.acs.org/10.1021/acsaelm.3c01804

Notes

The authors declare no competing financial interest.

■ ACKNOWLEDGMENTS

This work was supported by the National Science Foundation (ECCS-2105566) and the Air Force Office of Scientific Research under DURIP award no. FA9550-22-1-0505. The authors acknowledge the use of the XPS instrument at UC Riverside, which is supported by the National Science Foundation (DMR-0958796), and the use of facilities and instrumentation at the UC Irvine Materials Research Institute (IMRI), which is supported in part by the National Science Foundation through the UC Irvine Materials Research Science and Engineering Center (DMR-2011967).

■ REFERENCES

(1) Hosono, H.; Ueda, K. Transparent conductive oxides. *Springer Handbook of Electronic and Photonic Materials*; Springer, 2017; p 1.

(2) Hosono, H.; Ohta, H.; Orita, M.; Ueda, K.; Hirano, M. Frontier of transparent conductive oxide thin films. *Vacuum* **2002**, *66* (3−4), 419−425.

(3) Das, S.; Jayaraman, V. SnO2: A comprehensive review on structures and gas sensors. *Prog. Mater. Sci.* **2014**, *66*, 112−255.

(4) Barsan, N.; Schweizer-Berberich, M.; Göpel†, W. Fundamental and practical aspects in the design of nanoscaled SnO2 gas sensors: a status report. *Fresen. J. Anal. Chem.* **1999**, *365*, 287−304.

(5) Aukkaravittayapun, S.; Wongtida, N.; Kasecwatin, T.; Charojrochkul, S.; Unnanon, K.; Chindaudom, P. Large scale F-doped SnO2 coating on glass by spray pyrolysis. *Thin Solid Films* **2006**, *496* (1), 117−120.

(6) Olivi, P.; Pereira, E. C.; Longo, E.; Varella, J. A.; Bulhões, L. O. d. S. Preparation and characterization of a dip-coated SnO2 film for

transparent electrodes for transmissive electrochromic devices. *J. Electrochem. Soc.* **1993**, *140* (5), L81−L82.
(7) Yu, S.; Zhang, W.; Li, L.; Xu, D.; Dong, H.; Jin, Y. Optimization of SnO2/Ag/SnO2 tri-layer films as transparent composite electrode with high figure of merit. *Thin Solid Films* **2014**, *552*, 150−154.
(8) Zhou, W.; Liu, Y.; Yang, Y.; Wu, P. Band gap engineering of SnO2 by epitaxial strain: experimental and theoretical investigations. *J. Phys. Chem. C* **2014**, *118* (12), 6448−6453.
(9) Zhao, B.; Wang, F.; Chen, H.; Zheng, L.; Su, L.; Zhao, D.; Fang, X. An ultrahigh responsivity (9.7 mA W- 1) self-powered solar-blind photodetector based on individual ZnO-Ga2O3 heterostructures. *Adv. Funct. Mater.* **2017**, *27* (17), 1700264.
(10) Kaushik, S.; Naik, T. R.; Alka, A.; Garg, M.; Tak, B. R.; Ravikanth, M.; Rao, V. R.; Singh, R. Surface modification of AlN using organic molecular layer for improved deep UV photodetector performance. *ACS Appl. Electron. Mater.* **2020**, *2* (3), 739−746.
(11) Li, J.; Fan, Z.; Dahal, R.; Nakarmi, M.; Lin, J.; Jiang, H. 200nm deep ultraviolet photodetectors based on AlN. *Appl. Phys. Lett.* **2006**, *89* (21), 213510.
(12) Dahal, R.; Al Tahtamouni, T.; Lin, J.; Jiang, H. AlN avalanche photodetectors. *Appl. Phys. Lett.* **2007**, *91* (24), 243503.
(13) Guo, D.; Liu, H.; Li, P.; Wu, Z.; Wang, S.; Cui, C.; Li, C.; Tang, W. Zero-Power-Consumption Solar-Blind Photodetector Based on β-Ga_2O_3/NSTO Heterojunction. *ACS Appl. Mater. Interfaces* **2017**, *9* (2), 1619−1628.
(14) Chen, X.; Ren, F.; Gu, S.; Ye, J. Review of gallium-oxide-based solar-blind ultraviolet photodetectors. *Photon. Res.* **2019**, *7* (4), 381−415.
(15) Huang, L.; Feng, Q.; Han, G.; Li, F.; Li, X.; Fang, L.; Xing, X.; Zhang, J.; Hao, Y. Comparison Study of β-Ga2O3 Photodetectors Grown on Sapphire at Different Oxygen Pressures. *IEEE Photon. J.* **2017**, *9* (4), 1−8.
(16) Qin, Y.; Li, L. H.; Yu, Z.; Wu, F.; Dong, D.; Guo, W.; Zhang, Z.; Yuan, J. H.; Xue, K. H.; Miao, X.; et al. Ultra-high performance amorphous Ga2O3 photodetector arrays for solar-blind imaging. *Adv. Sci.* **2021**, *8* (20), 2101106.
(17) Qin, Y.; Li, L.; Zhao, X.; Tompa, G. S.; Dong, H.; Jian, G.; He, Q.; Tan, P.; Hou, X.; Zhang, Z.; et al. Metal-semiconductor-metal ε-Ga_2O_3 solar-blind photodetectors with a record-high responsivity rejection ratio and their gain mechanism. *ACS Photonics* **2020**, *7* (3), 812−820.
(18) Mishra, U. K.; Parikh, P.; Wu, Y.-F. AlGaN/GaN HEMTs-an overview of device operation and applications. *Proc. IEEE* **2002**, *90* (6), 1022−1031.
(19) Monroy, E.; Calle, F.; Pau, J.; Munoz, E.; Omnes, F.; Beaumont, B.; Gibart, P. AlGaN-based UV photodetectors. *J. Cryst. Growth* **2001**, *230* (3−4), 537−543.
(20) Li, D.; Jiang, K.; Sun, X.; Guo, C. AlGaN photonics: recent advances in materials and ultraviolet devices. *Adv. Opt. Photonics* **2018**, *10* (1), 43−110.
(21) Zhang, H.; Liang, F.; Song, K.; Xing, C.; Wang, D.; Yu, H.; Huang, C.; Sun, Y.; Yang, L.; Zhao, X.; et al. Demonstration of AlGaN/GaN-based ultraviolet phototransistor with a record high responsivity over 3.6×10^7 A/W. *Appl. Phys. Lett.* **2021**, *118* (24), 242105.
(22) Huang, C.; Zhang, H.; Sun, H. Ultraviolet optoelectronic devices based on AlGaN-SiC platform: Towards monolithic photonics integration system. *Nano Energy* **2020**, *77*, 105149.
(23) Chen, H.; Tan, C.; Sun, D.; Zhao, W.; Tian, X.; Huang, Y. Ultrawide range tuning of direct band gap in MgZnO monolayer via electric field effect. *RSC Adv.* **2018**, *8* (3), 1392−1397.
(24) Chen, X.; Ruan, K.; Wu, G.; Bao, D. Tuning electrical properties of transparent p-NiO/n-MgZnO heterojunctions with band gap engineering of MgZnO. *Appl. Phys. Lett.* **2008**, *93* (11), 112112.
(25) Shou, C.; Yang, T.; Almujtabi, A.; Yang, T.; Li, Y.; Mahmud, Q. S.; Xu, M.; Zheng, J.-G.; Liu, J. Improving crystal quality of β-phase MgGaO thin films by using low-temperature homo-buffer layer. *Appl. Phys. Lett.* **2023**, *122* (21), 212101.
(26) Yang, T.; Shou, C.; Almujtabi, A.; Tran, J.; Lin, Q.; Li, Y.; Mahmud, Q. S.; Wei, P.; Liu, J. Investigation of Phase Transition and Ultrawide Band Gap Engineering in MgGaO Semiconductor Thin Films. *ACS Appl. Opt. Mater.* **2023**, *1* (10), 1670−1678.
(27) Yang, T.; Shou, C.; Xu, L.; Tran, J.; He, Y.; Li, Y.; Wei, P.; Liu, J. Metal−Semiconductor−Metal Photodetectors Based on β-MgGaO Thin Films. *ACS Appl. Electron. Mater.* **2023**, *5* (4), 2122−2130.
(28) Ji, Z.; He, Z.; Song, Y.; Liu, K.; Ye, Z. Fabrication and characterization of indium-doped p-type SnO2 thin films. *J. Cryst. Growth* **2003**, *259* (3), 282−285.
(29) Ni, J.; Zhao, X.; Zheng, X.; Zhao, J.; Liu, B. Electrical, structural, photoluminescence and optical properties of p-type conducting, antimony-doped SnO2 thin films. *Acta Mater.* **2009**, *57* (1), 278−285.
(30) Scanlon, D. O.; Watson, G. W. On the possibility of p-type SnO 2. *J. Mater. Chem.* **2012**, *22* (48), 25236−25245.
(31) Rahal, A.; Benramache, S.; Benhaoua, B. Preparation of n-type semiconductor SnO2 thin films. *J. Semicond.* **2013**, *34* (8), 083002.
(32) Bendjedidi, H.; Attaf, A.; Saidi, H.; Aida, M.; Semmari, S.; Bouhdjar, A.; Benkhetta, Y. Properties of n-type SnO2 semiconductor prepared by spray ultrasonic technique for photovoltaic applications. *J. Semicond.* **2015**, *36* (12), 123002.
(33) Rastomjee, C.; Egdell, R.; Georgiadis, G.; Lee, M.; Tate, T. n-Type doping of SnO2 thin films by Sb ion implantation. *J. Mater. Chem.* **1992**, *2* (5), 511−520.
(34) Xu, C.; Wang, Z.; Lin, Z.; Chen, J.; Zheng, W. Band gap engineering of amorphous MgSnO film for deep-ultraviolet photodetection. *IEEE Electron Device Lett.* **2023**, *44* (2), 233−236.
(35) Nathan, A.; Lee, S.; Jeon, S.; Robertson, J. Amorphous oxide semiconductor TFTs for displays and imaging. *J. Disp. Technol.* **2014**, *10* (11), 917−927.
(36) Lu, B.; Zhuge, F.; Zhao, Y.; Zeng, Y.-J.; Zhang, L.; Huang, J.; Ye, Z.; Lu, J. Amorphous oxide semiconductors: From fundamental properties to practical applications. *Curr. Opin. Solid State Mater. Sci.* **2023**, *27*, 101092.
(37) Kamiya, T.; Hosono, H. Material characteristics and applications of transparent amorphous oxide semiconductors. *NPG Asia Mater.* **2010**, *2* (1), 15−22.
(38) Medvedeva, J. E.; Buchholz, D. B.; Chang, R. P. Recent advances in understanding the structure and properties of amorphous oxide semiconductors. *Adv. Electron. Mater.* **2017**, *3* (9), 1700082.
(39) Kuznetsov, M.; Safonov, A. Structural, optical, XPS, and magnetic properties of Sn-O nanoparticles. *Mater. Chem. Phys.* **2023**, *302*, 127739.
(40) Themlin, J.-M.; Chtaïb, M.; Henrard, L.; Lambin, P.; Darville, J.; Gilles, J.-M. Characterization of tin oxides by x-ray-photoemission spectroscopy. *Phys. Rev. B: Condens. Matter Mater. Phys.* **1992**, *46* (4), 2460−2466.
(41) Khairallah, F.; Glisenti, A.; Natile, M. M.; Galenda, A. CuO/MgO Nanocomposites by wet impregnation: an XPS study. *Surf. Sci. Spectra* **2012**, *19* (1), 23−29.
(42) Sadeghi, E.; Peighambardoust, N. S.; Khatamian, M.; Unal, U.; Aydemir, U. Metal doped layered MgB2 nanoparticles as novel electrocatalysts for water splitting. *Sci. Rep.* **2021**, *11* (1), 3337.
(43) Lu, Y.; Jiang, J.; Xia, C.; Kramm, B.; Polity, A.; He, Y.; Klar, P.; Meyer, B. The influence of oxygen flow rate on properties of SnO2 thin films grown epitaxially on c-sapphire by chemical vapor deposition. *Thin Solid Films* **2015**, *594*, 270−276.
(44) Dercz, G.; Prusik, K.; Pajak, L.; Pielaszek, R.; Malinowski, J. J.; Pudło, W. Structure studies on nanocrystalline powder of MgO xerogel prepared by the sol-gel method. *Mater. Sci.* **2009**, *27* (2), 201.
(45) Ke, C.; Yang, Z.; Zhu, W.; Pan, J.; Karamat, S. Heteroepitaxial growth of SnO2 thin films on SrTiO3 (111) single crystal substrate by laser molecular beam epitaxy. *J. Appl. Phys.* **2010**, *107* (1), 013515.
(46) Sze, S. M.; Li, Y.; Ng, K. K. *Physics of Semiconductor Devices*; John Wiley & Sons, 2021; p 159.
(47) Chiu, F.-C. A review on conduction mechanisms in dielectric films. *Adv. Mater. Sci. Eng.* **2014**, *2014*, 1−18.

https://doi.org/10.1021/acsaelm.3c01804
ACS Appl. Electron. Mater. 2024, 6, 1912−1920

(48) Pan, S.; Li, G. Recent progress in p-type doping and optical properties of SnO2 nanostructures for optoelectronic device applications. *Recent Pat. Nanotechnol.* **2011**, *5* (2), 138−161.
(49) Jeong, J.; Choi, S.-P.; Chang, C. I.; Shin, D. C.; Park, J. S.; Lee, B.; Park, Y.-J.; Song, H.-J. Photoluminescence properties of SnO2 thin films grown by thermal CVD. *Solid State Commun.* **2003**, *127* (9−10), 595−597.
(50) Di Bartolomeo, A.; Kumar, A.; Durante, O.; Sessa, A.; Faella, E.; Viscardi, L.; Intonti, K.; Giubileo, F.; Martucciello, N.; Romano, P.; et al. Temperature-dependent photoconductivity in two-dimensional MoS2 transistors. *Mater. Today Nano* **2023**, *24*, 100382.
(51) Hou, Q.; Liu, K.; Chen, X.; Yang, J.; Ai, Q.; Cheng, Z.; Zhu, Y.; Li, B.; Liu, L.; Shen, D. Effects of Mg Component Ratio on Photodetection Performance of MgGa2O4 Solar-Blind Ultraviolet Photodetectors. *Phys. Status Solidi Rapid Res. Lett.* **2022**, *16* (8), 2200137.
(52) Xie, F.; Gu, Y.; Hu, Z.; Yu, B.; Yang, G. Ultra-low dark current back-illuminated AlGaN-based solar-blind ultraviolet photodetectors with broad spectral response. *Opt. Express* **2022**, *30* (13), 23756−23762.
(53) Oh, S.; Kim, C.-K.; Kim, J. High Responsivity β-Ga_2O_3 Metal−Semiconductor−Metal Solar-Blind Photodetectors with Ultraviolet Transparent Graphene Electrodes. *ACS Photonics* **2018**, *5* (3), 1123−1128.
(54) Wang, Y.; Li, H.; Cao, J.; Shen, J.; Zhang, Q.; Yang, Y.; Dong, Z.; Zhou, T.; Zhang, Y.; Tang, W.; et al. Ultrahigh gain solar blind avalanche photodetector using an amorphous Ga2O3-based heterojunction. *ACS Nano* **2021**, *15* (10), 16654−16663.
(55) Zhang, Q.; Li, N.; Zhang, T.; Dong, D.; Yang, Y.; Wang, Y.; Dong, Z.; Shen, J.; Zhou, T.; Liang, Y.; et al. Enhanced gain and detectivity of unipolar barrier solar blind avalanche photodetector via lattice and band engineering. *Nat. Commun.* **2023**, *14* (1), 418.

https://doi.org/10.1021/acsaelm.3c01804
ACS Appl. Electron. Mater. 2024, 6, 1912−1920